First-principles simulations of scanning tunneling microscopy images exhibiting anomalous dot patterns on armchair-edged graphene nanoribbons

Junhuan Li ®,* Kouji Inagaki ®, and Kenta Arima ®

Department of Precision Engineering, Graduate School of Engineering, Osaka University, 2-1 Yamada-oka, Suita, Osaka 565-0871, Japan

To interpret our recent scanning tunneling microscopy (STM) experiment of nanographene sheets, in which the existence of rectangularlike lattices is confirmed, we conducted first-principles calculations of both simple and wrinkled armchair-edged graphene nanoribbons (AGNRs). We focused on the origin of this unique lattice and simulated STM images in the occupied band for the above-mentioned ribbons with different widths. Combined with the band structures of AGNRs, we investigated the features of electron distribution in detail under various magnitudes of applied sample biases (-1 to -0.05 V). In contrast to the well-known hexagonal structure of graphene at a large bias of -1 V, a rectangularlike lattice emerges in the STM images of AGNRs with specific widths when they are generated solely by electronic states occupying the valence band maximum. Furthermore, we find that a wrinkle in graphene parallel to the edges in AGNR significantly affects the STM images of a neighboring flat graphene region, even when its height is only several angstroms. By comparing the partial density of states of the wrinkle with flat graphene, we discussed the role of a wrinkle in functionalizing graphene sheets.

I. INTRODUCTION

The emergence of nanometer-sized graphene (nanographene) overcame graphene's gapless spectrum, which has direct application in field-effect transistors [1] and other semiconducting devices [2]. In addition to topological defects in nanographene that increase chemical interactions between the graphene surface and adsorbed molecules [3,4], significant attention has been paid to the use of defects to modulate its optical and mechanical properties [5,6]. Recent studies have shown that most of the chemical reactions occur at the edges or defective sites of graphene [7,8]. Therefore, to advance the design, preparation, and application of nanographene, understanding the effects of all kinds of defects on its electronic structures is highly desired.

Computations on armchair-edged graphene nanoribbons (AGNRs), such as simulations of scanning tunneling microscopy (STM) images, have been conducted for decades. As implied by calculations [9] on AGNRs, STM images representing electron density maps are exceedingly sensitive to local edge effects, which also provides a consistent description of the edge states of nanographene in experiments [10]. In these studies, the $\sqrt{3} \times \sqrt{3}$ superstructure is well known, representing an exclusive electronic structure resulting from electron scattering at the armchair edges. Due to this quantum

confinement and edge effects, AGNRs exhibit tunable and sizable energy gaps (Δ) [11]. Based on the number of carbon atom rows along their width (W), AGNRs are classified into $W = 3a-2$, $3a-1$, and $3a$ families, where a is an integer. For a particular value of a, the size of energy gaps obeys $\Delta_{3a-1} < \Delta_{3a} < \Delta_{3a-2}$. Not only energy gaps but also other electronic properties of AGNRs exhibit sensitivity to their width, as shown by Wassmann *et al.* [12] in simulated STM images. In their work, although simulated STM images of AGNRs with different widths all exhibited $\sqrt{3} \times \sqrt{3}$ phases, the electron density patterns undergo a threefold periodic variation with changes in the ribbon's width. However, in our previous STM observations [13] of nanographene sheets, a rectangularlike structure was discovered, which constitutes a novel superstructure not reported in the literature mentioned above. This rectangularlike structure is closely related in size and distribution to the $\sqrt{3} \times \sqrt{3}$ structure. Moreover, there has been a precedent [14] where the $\sqrt{3} \times \sqrt{3}$ structure appeared laterally overlapped to create a honeycomb superstructure near a kink of armchair edges. We believe that if two armchair edges face each other and are in close proximity, the $\sqrt{3} \times \sqrt{3}$ phases on both sides can vertically overlap to generate a rectangularlike structure. To verify this hypothesis, we successfully reproduced the rectangularlike structure in simulated STM images of AGNRs with a specific width of $W = 3a$ [13]. From surface observations of graphite several decades ago to the atomic-level precise synthesis of AGNRs today [15,16], nanographene has yielded significant results in both experimental and theoretical research. However, no description of the rectangularlike structure in this hexagonal carbon material has emerged. To address this gap, this paper aims to investigate the origin of the rectangularlike lattice and provide a comprehensive analysis of the electronic structure

---

*Corresponding author: j-li@sie.prec.eng.osaka-u.ac.jp

of AGNRs. We particularly focus on the dependence of STM images on the sample bias (V_s).

Next, in our previous experiments, the rectangular lattice was observed in the interior of the nanographene rather than AGNR. Recent reports highlight the edgelike role played by ripples and wrinkles in graphene. STM studies by Xu *et al.* [17] recognized that wrinkles or local curvature in exfoliated graphene monolayers induce a transition of the hexagonal carbon structure into a triangular pattern, indicating the broken sixfold symmetry. Wang *et al.* [18] demonstrated that "chemical cutting" enables the electronic properties of AGNRs in a large graphene sheet on C-faced terraces of SiC. It emphasizes the fact that graphene is strongly bonded to the exposed Si atoms on SiC sidewalls, named the "pinning region." These reports indicate that such line defects play a similar role to edges in STM images, which needs to be theoretically investigated.

In this study, we simulated the electronic structures of simple and wrinkled AGNRs using first-principles calculation. We performed calculations on their electronic structure properties, including band structures and simulated STM images. We suggest that the electronic structures of AGNRs are variable and strongly dependent on V_s. In the analysis of an introduced wrinkle, we demonstrate that the AGNR with wrinkle defects exhibits different electronic structures from those of simple AGNRs.

II. METHODS

A. Structural model

The graphene ribbons examined in this study were simple and wrinkled AGNRs. Both were treated as armchair edges with single hydrogen termination, which is one of the most thermodynamically stable structures [19]. AGNRs are the most studied graphene structures, where the band gap follows three different trends and shrinks with increasing width. For AGNRs with a wrinkle, a line defect is parallel to the edges.

An AGNR is specified by the number of dimer lines along the ribbon, forming the width W [11]. Figures 1(a) and 1(b) show schematic drawings of simple AGNRs with $W = 21$ and 39. According to the ribbon width, both belong to the $W = 3a$ family (*a* represents an integer). In other words, both have only one unique Clar representation with a maximal number of Clar sextets for their unit cell [12]. In this study, we refer to AGNRs with a width index W of 21 as 21-AGNR, and the same rule applies to AGNRs with other widths. Periodic boundary conditions were applied to a supercell setup with a length l_{cell}, as indicated by the bar above each schematic drawing. Calculations were performed for width indices in the range of $W = 21$–39, translating into widths ranging from 23.5 to 42.3 Å between the outermost hydrogen atoms.

B. Computational methods

Ab initio calculations were performed to analyze electronic structures using the program package STATE [20] with plane-wave basis functions, ultrasoft pseudopotentials, and an exchange-correlation functional in the generalized-gradient approximation (GGA). A k-point sampling of 30 k points uniformly positioned along the one-dimensional (1D) Brillouin
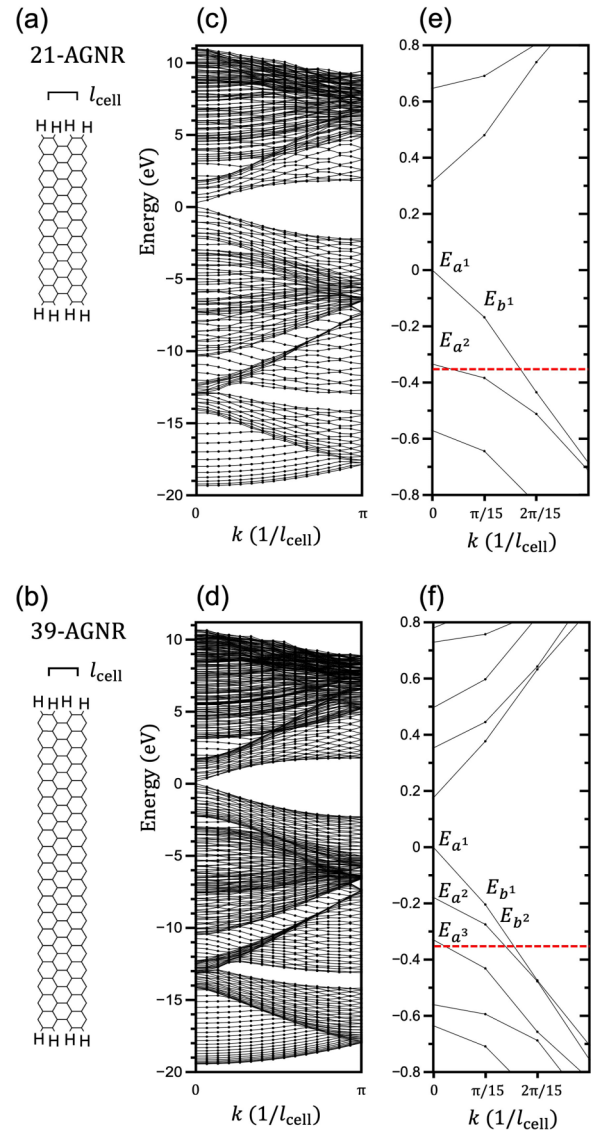

FIG. 1. Ribbon configurations and band structures of 21-AGNR and 39-AGNR. Note that only the σ-bond network between carbon atoms is depicted in (a) and (b). The band structures of 21-AGNR and 39-AGNR are plotted in (c) and (d). The bands close to ε_{HOMO} are depicted in (e) and (f). Eigenvalues at $k = 0$ and its neighbor ($k = \frac{\pi}{15}/l_{cell}$) are denoted by E_{a^n} and E_{b^n}. Zero of energy is set to ε_{HOMO}.

zone is employed for AGNRs. Calculations with a sampling of 100 k points as a comparison are provided in the Appendix. The cutoff energy for the wave functions was set to 36 Ry, and one for the charge to 400 Ry. In our supercell setup, vacuum distances of 15.9 and 10.6 Å separated the ribbons in plane and between planes. Lattice constants and internal coordinates for simple AGNRs (without wrinkle) were optimized and allowed to relax down to a force threshold of 10^{-3} a.u. Details regarding the structural optimization of the AGNR with a wrinkle will be discussed later.

With optimized coordinates, STM images were simulated for AGNRs and obtained as energy-integrated local density of states (LDOS), as proposed by the Tersoff-Hamann approximation [21]. In our calculations, we attempt to understand

TABLE I. Eigenvalues involved in computing STM images at different sample biases (V_s).

V_s	−0.05 V	−0.19 V	−0.24 V	−0.29 V	−0.35 V
21-AGNR	E_{a^1}	E_{a^1}	E_{a^1}	E_{a^1}	E_{a^1}
		E_{b^1}	E_{b^1}	E_{b^1}	E_{b^1}
					E_{a^2}
39-AGNR	E_{a^1}	E_{a^1}	E_{a^1}	E_{a^1}	E_{a^1}
		E_{a^2}	E_{a^2}	E_{a^2}	E_{a^2}
			E_{b^1}	E_{b^1}	E_{b^1}
				E_{b^2}	E_{b^2}
					E_{a^3}

how the distribution of electrons with high energies influences STM images. In other words, the bias dependence on images was investigated in a small and negative bias region. To avoid inaccuracy in the Fermi level (ε_F), we used the sum of the electron density of orbitals in [$\varepsilon_{HOMO} + eV_s$, ε_{HOMO}] for a negative V_s, where e denotes the elementary charge ($e > 0$) and ε_{HOMO} denotes the energy level of the highest occupied molecular orbital (HOMO). Computed LDOS contours were obtained for the simulated STM images at the corresponding V_s.

III. RESULTS AND DISCUSSION

A. Band structures

Figure 1 depicts the ribbon configurations and band structures of 21-AGNR [Figs. 1(a), 1(c), and 1(e)] and 39-AGNR [Figs. 1(b), 1(d), and 1(f)]. In addition to 21-AGNR and 39-AGNR, we calculated the band structures of AGNRs belonging to other families. The trend of the energy gaps (E_g) is in accordance with previous work [11,22]. Magnified band structures near ε_{HOMO} for these two ribbons are depicted in Figs. 1(e) and 1(f). For 21-AGNR shown in Fig. 1(e), we notice an energy gap of 0.32 eV separating the valence and conduction bands. With the width index increasing to 39, Fig. 1(f) shows E_g shrinking to 0.17 eV. The red dotted lines indicate the energy of −0.35 eV, corresponding to V_s of −0.35 V. Three and five eigenvalues lie within 0.35 eV beneath the

ε_{HOMO} for 21-AGNR and 39-AGNR. Here, eigenvalues at $k = 0$ are represented as E_{a^n}, where a higher n indicates an eigenvalue at a lower energy level below the HOMO. Similarly, those at its neighbor $k = \frac{\pi}{15}/l_{cell}$ are defined as E_{b^n}.

In our previous paper [13], we compared the experimental data of graphene nanosheets with simulated STM images at V_s (−0.05 V). Based on this precedence result, we systematically investigate the effect of V_s near the ε_F on simulated STM images. The V_s values are listed in Table I. At each V_s, the number of eigenvalues (E_{a^n} and E_{b^n} in Fig. 1) involved in simulating STM images for 39-AGNR is at least equal to or even larger than that for 21-AGNR. That is because 39-AGNR has more atoms than 21-AGNR, resulting in more discrete energy values. For all V_s in Table I, we computed STM images to assess the impact of V_s on the images.

B. Simulated STM images

Figure 2 depicts the simulated STM images at V_s shown in Table I. At the minimum V_s of −0.05 V, only one eigenvalue (E_{a^1}) was responsible for the electron distribution, as listed in Table I. A rectangularlike pattern runs through the entire 21-AGNR and 39-AGNR widths, which is superimposed in Figs. 2(a) and 2(b). In our previous report [13], this particular lattice was observed in the STM experiments of graphene nanosheets at a low and negative V_s.

For 21-AGNR at V_s of −0.19 V, as shown in Fig. 2(c), the vertices of the rectangularlike lattice changed dramatically and transformed into a ringlike shape. This change is caused by the participation of E_{b^1} in the simulated image. For 39-AGNR at V_s of −0.19 V, as shown in Fig. 2(d), due to the added eigenvalue of E_{a^2}, which is not E_{b^1} as in the case of 21-AGNR, the STM image looks more like a hexagon near the center of the ribbon. Additionally, Fig. 2(d) reveals that the pattern near the edges is different from the hexagonal one at the center whose trend is not obvious for 21-AGNR in Fig. 2(c). This probably originates from the difference in width between these ribbons.

After V_s was increased up to −0.29 V for 21-AGNR, no new eigenvalues in Table I were added to compute STM images, resulting in no changes in Figs. 2(c), 2(e), and 2(g). For 39-AGNR, new eigenvalues E_{b^1} and E_{b^2} were included when
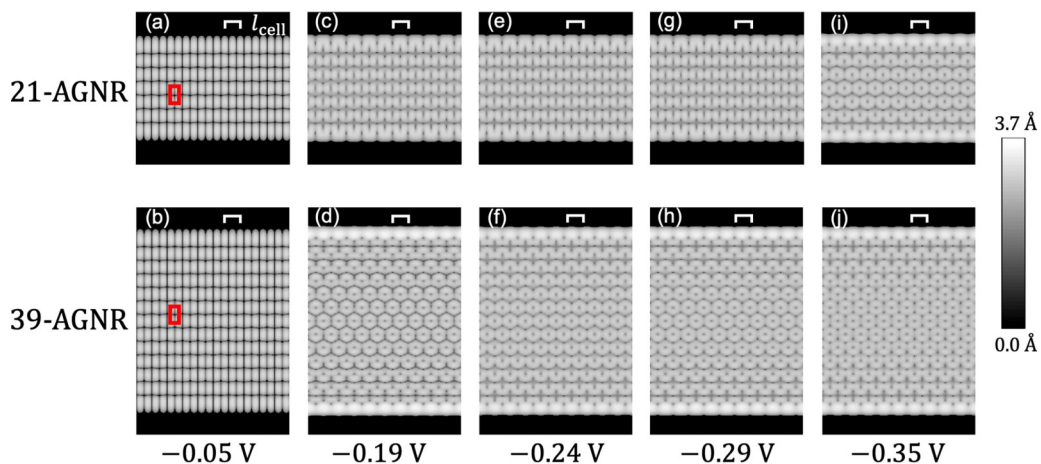

FIG. 2. STM images were simulated for 21-AGNR and 39-AGNR at V_s listed in Table I.

V_s increased from -0.19 to -0.24 V and from -0.24 to -0.29 V. In Fig. 2(f), the corrugation of the hexagon in the ribbon center becomes slightly blurred compared with Fig. 2(d). The simulated STM image in Fig. 2(h) is similar to the one in Fig. 2(f), indicating that E_{b^2} has little effect on the formation of STM images. Figure 2(i) showing 21-AGNR at V_s of -0.35 V resembles Fig. 2(f) showing 39-AGNR at V_s of -0.24 V, probably because the same eigenvalues (E_{a^1}, E_{b^1}, and E_{a^2}) contributed to the image formation for both ribbons even at different V_s values. In Fig. 2(j), the addition of E_{a^3} caused a slight change in the image. Namely, the ringlike shapes do not have a demarcation as clear as the ones at V_s of -0.29 V in Fig. 2(h).

A general trend in Fig. 2 is that eigenvalues with high energies in the occupied states significantly influence computed STM images. The simulated STM images of AGNRs with $W = 3a$ exhibit a unique rectangularlike lattice with E_{a^1}. Other eigenvalues with high energies, such as E_{a^2} and E_{b^1}, can affect the simulated STM images to some extent, which depends on how close they are to ε_{HOMO}. Although only the eigenvalues at $k = 0$ and 0.033 (or $k = \frac{\pi}{15}/l_{cell}$) are counted in Fig. 2, we have considered other k sites to check the simulated STM images in the Appendix. Again, as mentioned above, our conclusion is that only eigenvalues with high energies significantly influence our calculations, which remains unchanged even if k points were increased from 30 up to 100.

We show the simulated STM results of 37-, 38-, and 39-AGNRs belonging to all three families ($W = 3a-2$, $3a-1$, and $3a$) in Figs. 3(a)–3(d), 3(e)–3(h), and 3(i)–3(l). For every AGNR in Fig. 3, as the absolute value of V_s increases, the corrugations representing electron distributions always change. Furthermore, a comparison of AGNRs with different widths at the same V_s is shown in Fig. 3. At a minimum V_s of -0.05 V, the AGNRs of the three families exhibit different electronic structures. Figures 3(a) and 3(e) show STM images at this low V_s for 37-AGNR and 38-AGNR, which exhibit two different $(\sqrt{3} \times \sqrt{3})R30°$ superstructures. For 39-AGNR shown in Fig. 3(i), the STM image shows an entirely different rectangularlike lattice; these differences between varied families become less pronounced with increasing V_s, which also indicates that the electrons at the top of the valence band are more capable of changing the electronic structure of AGNRs. Figures 3(c), 3(g), and 3(k) show minor variations in STM images for different AGNRs calculated at a V_s of -0.5 V, which is inconsistent with previous reports [12,23]. This is probably because the AGNR widths in our study are wider, almost twice as much as those in previous studies. Figures 3(d), 3(h), and 3(l) show the results obtained at a V_s of -1 V, where more eigenvalues are involved than those in other images in Fig. 3. Here, Figs. 3(d), 3(h), and 3(l) show hexagonal patterns, as examples are depicted in red. This shows that STM images at large V_s lose the periodic change of dot patterns depending on the category of ribbon width ($W = 3a-2$, $3a-1$, and $3a$). They reflect the structure of an in-plane graphene network instead. In addition, bright dot patterns are obtained at the edges among all three images. These features at large V_s agree with a previous report [24]. In other words, obtaining an image at a small negative V_s is effective to distinguish the three families ($W = 3a-2$, $3a-1$, and $3a$) of AGNRs in experiments.
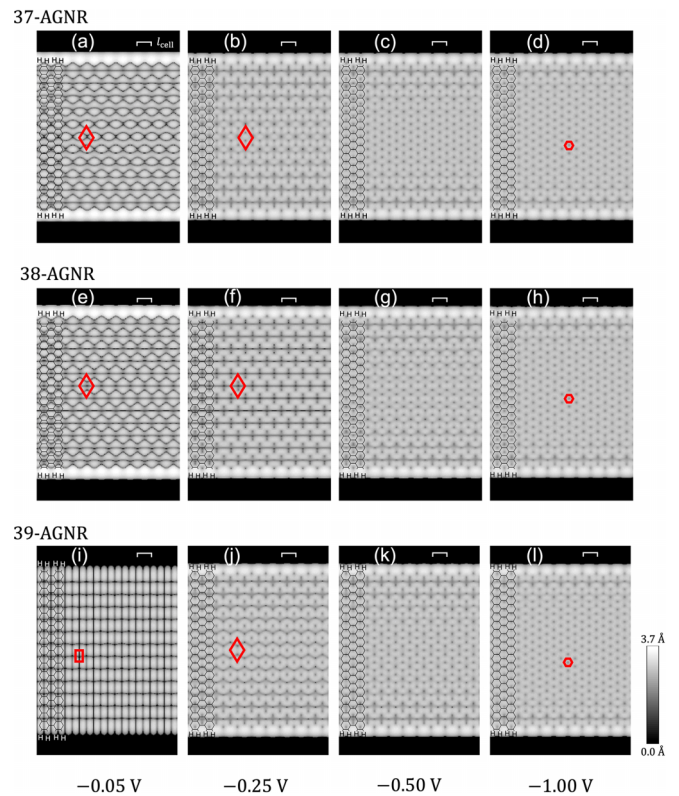

FIG. 3. Simulated STM images of AGNRs with three different families as 37-AGNR (upper), 38-AGNR (middle), and 39-AGNR (lower). STM images in each column were calculated using the V_s value below. The ribbon configurations are superimposed in each image.

C. A wrinkle in AGNRs

A graphene wrinkle was introduced into AGNRs. Wrinkling is a typical defect structure generated in two-dimensional materials on a supporting substrate [25,26]. In this paper, we abbreviate nanowrinkles on graphene, or graphene nanowrinkles, as GNWs. Recent experimental data on graphene sheets with GNWs show some new findings, such as its 1D electron confinement [27,28]. However, little is known about the structural morphology and electronic properties of GNWs due to two main reasons: one is that wrinkles are easily deformed due to external influences, and they will fold over after reaching a maximum of $\sim$6 nm [29]. The other is that measurements are always performed on the substrate; thus, the intrinsic effect of the interaction with a substrate cannot be ignored.

To eliminate the effects of a substrate, we investigated the electronic structure of a freestanding AGNR with a wrinkled defect. Using the model shown in Fig. 4, we examine how a GNW in an AGNR affects STM images at low V_s. The relaxed model of 37-AGNR, with which we simulated the electron density maps in Figs. 3(a)–3(d), was used as the starting material. Note that the C atoms in this simple AGNR are all distributed in the same plane. In the following, x and y axes in-plane were taken parallel and perpendicular to the armchair edge. The z axis was taken as the direction normal to the plane. To make the 37-AGNR bent in Fig. 4(a), we kept the flat portion in-plane fixed and separately optimized
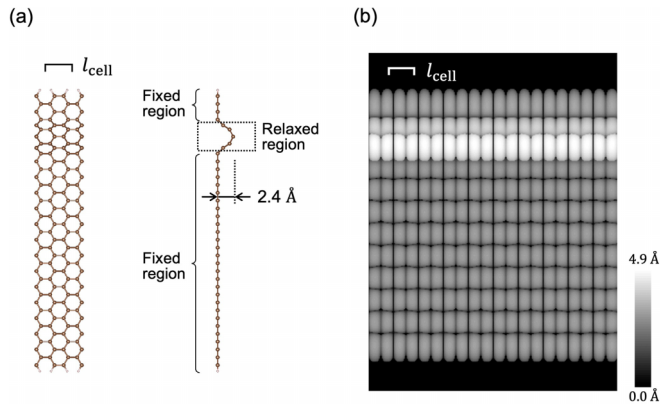
FIG. 4. 37-AGNR with a wrinkle. (a) The ball and stick models; the edges of the ribbon are terminated by hydrogen atoms (small balls). Braces and the dashed box indicate the fixed atoms and the relaxed atoms, respectively. The wrinkle has a height of 2.4 Å. (b) Simulated image of this AGNR with a V_s of -0.05 V.

the structure of the wrinkled part in Fig. 4(a). The wrinkled structure was allowed to relax down to a force threshold of 10^{-3} a.u. To reproduce the experiments in Ref. [13], the model in Fig. 4(a) has a GNW with a straight ridge with a limited height of 2.4 Å in the z axis. We emphasize that the linear wrinkle in our model is parallel to the top and bottom edges. The typical height and width of the wrinkle in 37-AGNR are comparable to the measured [27] and calculated [30] values in other studies. As illustrated in Figs. 3(a), 3(e), and 3(i), only the STM images of AGNRs at low V_s exhibit the periodic change with respect to the three families ($W = 3a-2$, $3a-1$, and $3a$). Thus, we calculated the STM image at -0.05 V in

Fig. 4(b). In contrast to the rhombus lattices on the simple 37-AGNR shown in Fig. 3(a), rectangularlike lattices similar to those in Fig. 3(i) are visible on the AGNR with a wrinkle shown in Fig. 4(b).

In Fig. 4, we demonstrated that GNW changes the STM image representing the distribution of electrons with high energies in the occupied band. This is probably because the wrinkled structure in Fig. 4(a) disturbs the resonance [12] of the electron distributions determined by the ribbon width, which is $W = 3a-2$ in this case. We also conducted similar calculations to those in Fig. 4 with wrinkled graphene, where we varied the width, height, and position of the wrinkle. Unfortunately, as these structural parameters are extensive, we have not completed a systematic study on how each parameter of the wrinkle affects the electronic structure on a flat graphene region. It should be noted that what we observe in Fig. 4 is that a wrinkle parallel to the armchair edges alters the electron distribution on a neighboring flat graphene region, even if the wrinkle's height is only a few angstroms.

In our experimental work, rectangular lattices were found on nanographene sheets. We speculate that the wrinkled structure played the role of an edge, altering the electronic distribution of these nanographene sheets. If two line defects, such as edges or wrinkles whose ridges are sufficiently high, were parallel and in close proximity, the electronic structure of AGNRs appeared in the region between these line defects, even on graphene sheets that are not perfect ribbons. In Fig. 4, the rectangularlike lattices appear in 37-AGNR with a wrinkle, which directly proves the above-mentioned perspectives.

Finally, the effect of introduced wrinkles on the density of states (DOS) is worth mentioning, and the calculated results
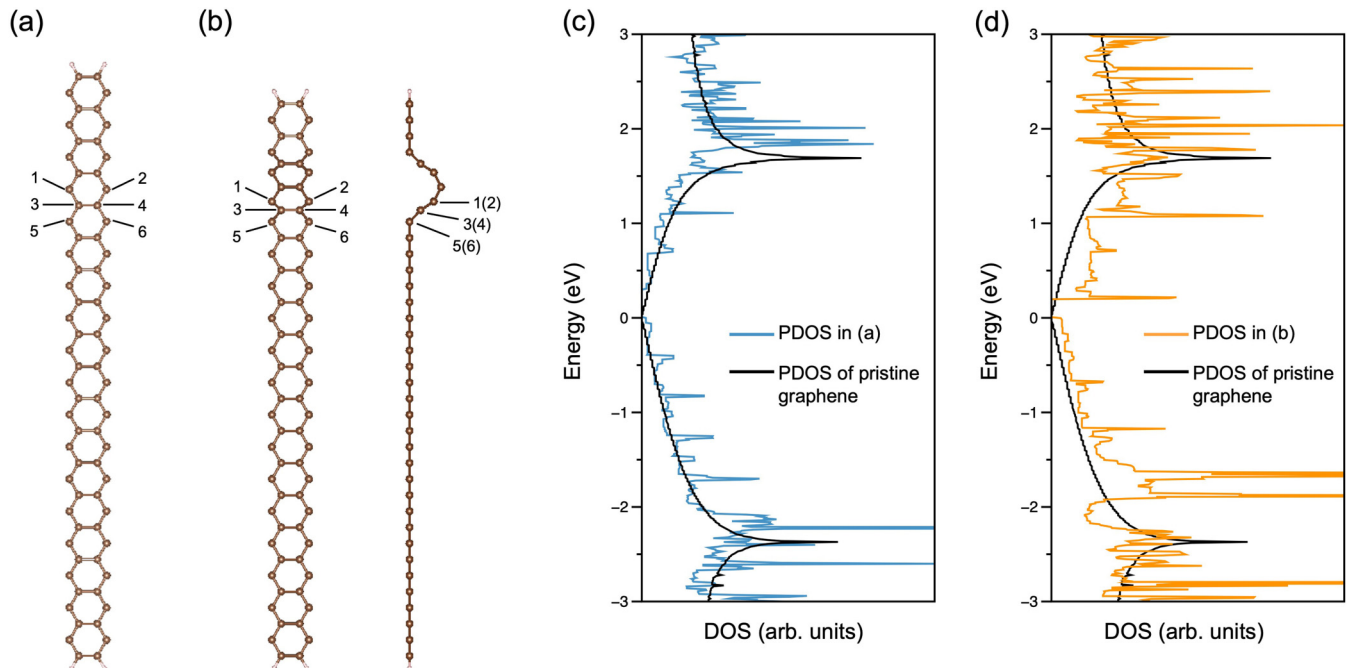

FIG. 5. PDOS of the simple 37-AGNR and the one with a wrinkled structure. (a) Schematic of simple 37-AGNR. (b) Schematic of wrinkled 37-AGNR. The notation "1(2)" indicates two atoms labeled as 1 and 2 in the left panel, and the same rule applies to 3(4) and 5(6). (c) PDOS of the six-labeled carbon atoms in (a). (d) PDOS of the six-labeled carbon atoms in (b). In (c) and (d), the PDOS of six carbon atoms in pristine graphene is also shown as black curves though its computational model is not provided.

are shown in Fig. 5. Six C atoms in Fig. 5(a) are in the same z plane, whereas the six C atoms in Fig. 5(b) are in a wrinkle configuration. The partial density of states (PDOS) of these C atoms are displayed in Figs. 5(c) and 5(d). For the six C atoms in the simple 37-AGNR, the contribution of the PDOS in Fig. 5(c) is similar to the PDOS in pristine graphene. In comparison to the PDOS of pristine graphene or the simple 37-AGNR, the PDOS of the wrinkled structure in Fig. 5(b) exhibits a significant contribution near 0 eV as shown in Fig. 5(d). A noticeable increase in electron or state density was shown in the energy ranges of $(-2$ eV, -1 eV) and $(0$ eV, 1 eV), along with a small increase in the range of $(-1$ eV, 0 eV). A high DOS in this energy range has also been proposed on the surface of nitrogen-doped graphene, which causes spontaneous adsorption of gas molecules and paves the way for subsequent chemical reactions [31,32]. Wang *et al.* demonstrated that morphology regulation could create wrinkles in graphene nanosheets as powerful adsorptive sites and remove organic pollutants [33]. The multicurved, wrinkled surface of graphene-based materials provides good lithium adsorption sites, resulting in improved lithium storage capability as a working anode [34]. In these reports, wrinkled surface defects improve the chemical activity of graphene, which is thought to be due to the high DOS near 0 eV shown in Fig. 5(d).

IV. SUMMARY

We performed first-principles calculations within the GGA approximation to obtain the band structures and STM images of AGNRs. The features in simulated STM images of AGNRs are found to be V_s sensitive, and this gives rise to three families of AGNRs based on the calculations of small V_s values. Specifically, at the top of the valence band, eigenvalues have a significant effect on STM images computed at the corresponding V_s. AGNRs with the width index $W = 3a$ exhibit a unique rectangularlike lattice when only the highest eigenvalue in the occupied states is calculated, which is the minimum V_s in this study. For the AGNRs of all three families, at this small V_s, triple periodicity according to the width is revealed. As the absolute V_s value increases, the STM images of all AGNRs change. When V_s reaches a sufficiently large value such as -1 V, the AGNRs of all three families exhibit the same hexagonal lattice, which is also consistent with previous studies. When a linear wrinkled defect is introduced into AGNRs, it plays a role similar to that of an edge, thereby changing the electronic structure or STM images in AGNRs. For instance, the above-mentioned rectangularlike lattice appears in 37-AGNR that does not belong to $W = 3a$. An increasing PDOS of the wrinkled structure was also displayed near the ε_F. Our computational method provides an approach for gaining insights into wrinkle defects in graphene. This enables a deeper
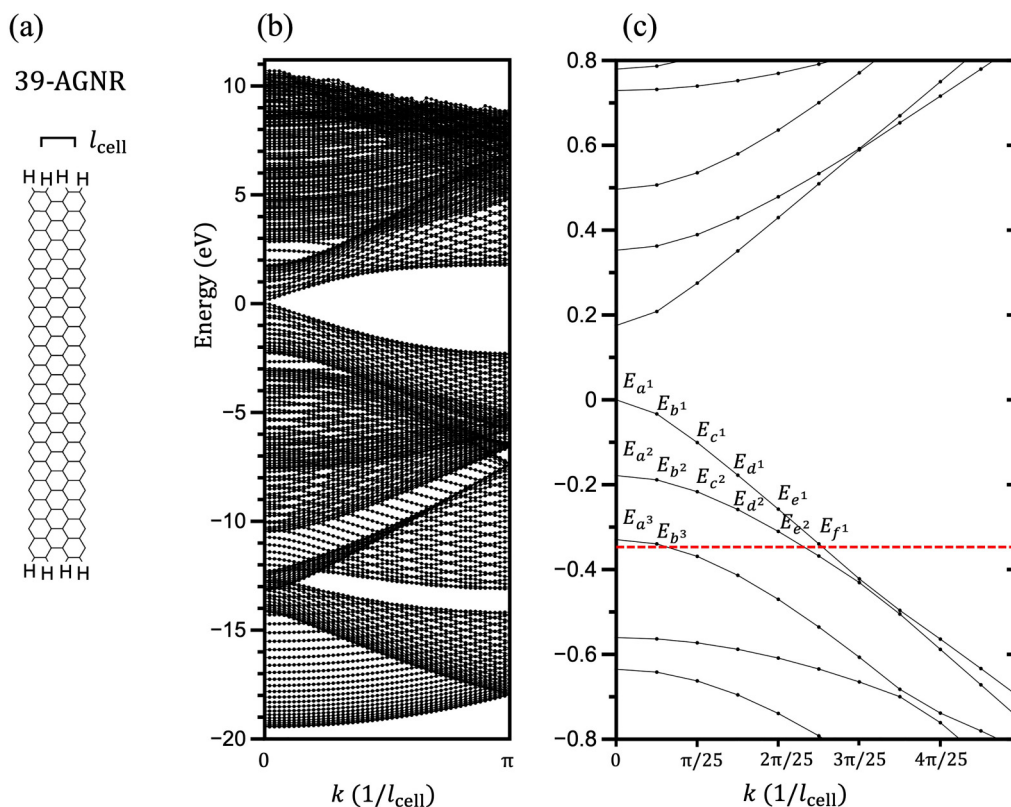

FIG. 6. Ribbon configuration and its band structures of 39-AGNR. k-point sampling of 100 k points is used; the red dotted line denotes the energy of -0.35 eV.

TABLE II. Eigenvalues involved in computing STM images of 39-AGNR at different V_s ranges in (a) and (b).

	(a)					
V_s	-0.030 V	-0.035 V	-0.105 V	-0.178 V	-0.180 V	-0.190 V
Eigenvalues	E_{a^1} E_{b^1}	E_{a^1} E_{b^1}	E_{a^1} E_{b^1} E_{c^1}	E_{a^1} E_{b^1} E_{c^1} E_{d^1}	$E_{a^{1\text{-}2}}$ E_{b^1} E_{c^1} E_{d^1}	$E_{a^{1\text{-}2}}$ $E_{b^{1\text{-}2}}$ E_{c^1} E_{d^1}

	(b)					
V_s	-0.220 V	-0.258 V	-0.260 V	-0.315 V	-0.330 V	-0.340 V
Eigenvalues	$E_{a^{1\text{-}2}}$ $E_{b^{1\text{-}2}}$ $E_{c^{1\text{-}2}}$ E_{d^1}	$E_{a^{1\text{-}2}}$ $E_{b^{1\text{-}2}}$ $E_{c^{1\text{-}2}}$ E_{d^1} E_{e^1}	$E_{a^{1\text{-}2}}$ $E_{b^{1\text{-}2}}$ $E_{c^{1\text{-}2}}$ $E_{d^{1\text{-}2}}$ E_{e^1}	$E_{a^{1\text{-}2}}$ $E_{b^{1\text{-}2}}$ $E_{c^{1\text{-}2}}$ $E_{d^{1\text{-}2}}$ $E_{e^{1\text{-}2}}$	$E_{a^{1\text{-}3}}$ $E_{b^{1\text{-}2}}$ $E_{c^{1\text{-}2}}$ $E_{d^{1\text{-}2}}$ $E_{e^{1\text{-}2}}$	$E_{a^{1\text{-}3}}$ $E_{b^{1\text{-}3}}$ $E_{c^{1\text{-}2}}$ $E_{d^{1\text{-}2}}$ $E_{e^{1\text{-}2}}$ E_{f^1}

understanding of the wrinkled structure and a more flexible use of this defect for graphene modification.

APPENDIX: SIMULATION OF 39-AGNR USING A 100 k-POINTS SAMPLING

In the following Appendix, we present density functional theory simulations of 39-AGNR (armchair-edged graphene nanoribbon). To check whether different k-point samplings would have an impact on our calculation, we used a k-point sampling of 100 k points, which is more than 30 k points in the main text. Other computational details are provided in the main text.

The 39-AGNR configuration with single hydrogen termination is depicted in Fig. 6(a). After self-consistent field calculation, the overall band structure, and its details at a specific k range, are depicted in Figs. 6(b) and 6(c), respectively. Similar to the case of the calculation with a 30 k-point sampling in the main text, an energy gap of 0.17 eV was shown in the band structures for 39-AGNR in Figs. 6(b) and 6(c). Compared to the main text, Fig. 6(c) shows a larger number of eigenvalues lying within 0.35 eV beneath the energy level of the highest occupied molecular orbital ($\varepsilon_{\text{HOMO}}$). The naming conventions for eigenvalues are provided in the main text. Notably, the eigenvalues in the Appendix, such as E_{b^1}, are different from those in the main text (except for E_{a^n}, which is at $k = 0$ in the main text and the Appendix).

Table II lists a set of V_s, along with the eigenvalues involved between the $\varepsilon_{\text{HOMO}}$ and each V_s. To save space, we use $E_{a^{1\text{-}2}}$ to denote E_{a^1} and E_{a^2}, and so on.
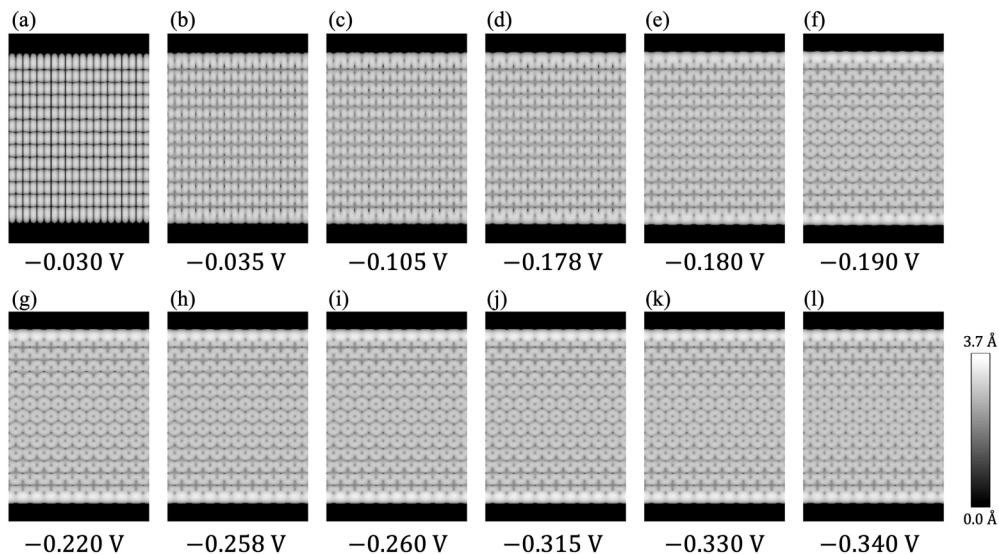
FIG. 7. STM images were simulated for 39-AGNR at V_s listed in Table II.

We simulate STM images of 39-AGNR (width index W of 39, belonging to $W = 3a$, where a represents an integer) in Fig. 7, using V_s listed in Table II. At the minimum V_s of -0.030 V in Fig. 7(a), a rectangularlike pattern was visible. In Fig. 7(f), we used the same V_s as in Fig. 2(d) of the main text, -0.190 V, which contributed to the same simulated STM image. Figures 7(b)–7(e) show the V_s between -0.030 and -0.190 V, containing eigenvalues absent in the main text. As the V_s value increases in this range, the rectangularlike structure gradually disappears. When the V_s value exceeded -0.190 V in Figs. 7(g)–7(l), the features of the STM images gradually stabilized and had a hexagonal structure. In conclusion, the results in Fig. 7 are consistent with the calculation in the main text. The simulated STM image of AGNRs with $W = 3a$ exhibits a unique rectangularlike lattice with E_{a^1}. Eigenvalues with high energies in the occupied states can significantly influence features in STM images.

[1] X. Li, X. Wang, L. Zhang, S. Lee, and H. Dai, Chemically derived, ultrasmooth graphene nanoribbon semiconductors, Science **319**, 1229 (2008).

[2] Z. Xu, Q. S. Zheng, and G. Chen, Elementary building blocks of graphene-nanoribbon-based electronic devices, Appl. Phys. Lett. **90**, 223115 (2007).

[3] N. Dimakis, I. Salas, L. Gonzalez, O. Vadodaria, K. Ruiz, and M. I. Bhatti, Li and Na adsorption on graphene and graphene oxide examined by density functional theory, quantum theory of atoms in molecules, and electron localization function, Molecules **24**, 754 (2019).

[4] C. U. Mendoza-Domínguez and V. A. Basiuk, Distortion and bonding strength of phthalocyanine molecules adsorbed on topological defects in graphene, Mater. Chem. Phys. **271**, 124963 (2021).

[5] H. Hu, J. H. Xin, H. Hu, X. Wang, and Y. Kong, Metal-free graphene-based catalyst-insight into the catalytic activity: A short review, Appl. Catal. A **492**, 1 (2015).

[6] L. Yan, Y. Zheng, F. Zhao, S. Li, X. Gao, B. Xu, P. S. Weiss, and Y. Zhao, Chemistry and physics of a single atomic layer: Strategies and challenges for functionalization of graphene and graphene-based materials, Chem. Soc. Rev. **41**, 97 (2012).

[7] L. Zhang, Q. Xu, J. Niu, and Z. Xia, Role of lattice defects in catalytic activities of graphene clusters for fuel cells, Phys. Chem. Chem. Phys. **17**, 16733 (2015).

[8] X. Zhang, J. Xin, and F. Ding, The edges of graphene, Nanoscale **5**, 2556 (2013).

[9] P. L. Giunta and S. P. Kelty, Direct observation of graphite layer edge states by scanning tunneling microscopy, J. Chem. Phys. **114**, 1807 (2001).

[10] Y. Kobayashi, K. Fukui, and T. Enoki, Edge state on hydrogen-terminated graphite edges investigated by scanning tunneling microscopy, Phys. Rev. B **73**, 125415 (2006).

[11] L. Yang, C. H. Park, Y. W. Son, M. L. Cohen, and S. G. Louie, Quasiparticle energies and band gaps in graphene nanoribbons, Phys. Rev. Lett. **99**, 186801 (2007).

[12] T. Wassmann, A. P. Seitsonen, A. M. Saitta, M. Lazzeri, and F. Mauri, Clar's theory, π-electron distribution, and geometry of graphene nanoribbons, J. Am. Chem. Soc. **132**, 3440 (2010).

[13] J. Li, S. Li, T. Higashi, K. Kawai, K. Inagaki, K. Yamamura, and K. Arima, Atomic-scale insights into the origin of rectangular lattice in nanographene probed by scanning tunneling microscopy, Phys. Rev. B **103**, 245433 (2021).

[14] W. Zhang, Z. Ju, and W. Wu, Intrinsic superstructure near atomically clean armchair step edges of graphite, Phys. Rev. B **100**, 115120 (2019).

[15] J. Cai, P. Ruffieux, R. Jaafar, M. Bieri, T. Braun, S. Blankenburg, M. Muoth, A. P. Seitsonen, M. Saleh, X. Feng, K. Müllen, and R. Fasel, Atomically precise bottom-up fabrication of graphene nanoribbons, Nature (London) **466**, 470 (2010).

[16] Y.-C. Chen, D. G. de Oteyza, Z. Pedramrazi, C. Chen, F. R. Fischer, and M. F. Crommie, Tuning the band gap of graphene nanoribbons synthesized from molecular precursors, ACS Nano **7**, 6123 (2013).

[17] K. Xu, P. Cao, and J. R. Heath, Scanning tunneling microscopy characterization of the electrical properties of wrinkles in exfoliated graphene monolayers, Nano Lett. **9**, 4446 (2009).

[18] W. Wang, M. Zhou, X. Li, S. Li, X. Wu, W. Duan, and L. He, Energy gaps of atomically precise armchair graphene sidewall nanoribbons, Phys. Rev. B **93**, 241403(R) (2016).

[19] T. Wassmann, A. P. Seitsonen, A. M. Saitta, M. Lazzeri, and F. Mauri, Structure, stability, edge states, and aromaticity of graphene ribbons, Phys. Rev. Lett. **101**, 096402 (2008).

[20] Y. Morikawa, K. Iwata, and K. Terakura, Theoretical study of hydrogenation process of formate on clean and Zn deposited Cu(111) surfaces, Appl. Surf. Sci. **169**, 11 (2001).

[21] J. Tersoff and D. R. Hamann, Theory of the scanning tunneling microscope, Phys. Rev. B **31**, 805 (1985).

[22] Y. W. Son, M. L. Cohen, and S. G. Louie, Energy gaps in graphene nanoribbons, Phys. Rev. Lett. **97**, 216803 (2006).

[23] H. Huang, D. Wei, J. Sun, S. L. Wong, Y. P. Feng, A. H. C. Neto, and A. T. S. Wee, Spatially resolved electronic structures of atomically precise armchair graphene nanoribbons, Sci. Rep. **2**, 1 (2012).

[24] J. Yamaguchi, H. Hayashi, H. Jippo, A. Shiotari, M. Ohtomo, M. Sakakura, N. Hieda, N. Aratani, M. Ohfuchi, Y. Sugimoto, H. Yamada, and S. Sato, Small bandgap in atomically precise 17-atom-wide armchair-edged graphene nanoribbons, Commun. Mater. **1**, 36 (2020).

[25] M. C. Wang, J. Leem, P. Kang, J. Choi, P. Knapp, K. Yong, and S. Nam, Mechanical instability driven self-assembly and architecturing of 2D materials, 2D Mater. **4**, 022002 (2017).

[26] J. A. Baimova, E. A. Korznikova, S. V. Dmitirev, B. Liu, and K. Zhou, Wrinkles and wrinklons in graphene and graphene nanoribbons under strain, Curr. Nanosci. **12**, 184 (2016).

[27] H. Lim, J. Jung, R. S. Ruoff, and Y. Kim, Structurally driven one-dimensional electron confinement in sub-5-nm graphene nanowrinkles, Nat. Commun. **6**, 8601 (2015).

[28] L. Liu, W. Xiao, D. Wang, K. Yang, L. Tao, and H. J. Gao, Edge states of graphene wrinkles in single-layer

graphene grown on Ni(111), Appl. Phys. Lett. **109**, 143103 (2016).

[29] W. Zhu, T. Low, V. Perebeinos, A. A. Bol, Y. Zhu, H. Yan, J. Tersoff, and P. Avouris, Structure and electronic transport in graphene wrinkles, Nano Lett. **12**, 3431 (2012).

[30] Y. Guo and W. Guo, Electronic and field emission properties of wrinkled graphene, J. Phys. Chem. C **117**, 692 (2013).

[31] X. Li, W. Hua, J. Guo, and Y. Luo, Electronic structure of nitrogen-doped graphene in the ground and core-excited states from first-principles simulations, J. Phys. Chem. C **119**, 16660 (2015).

[32] Y. Liu, B. Song, C. Huang, and L. Yang, Dual transition metal atoms embedded in N-doped graphene for electrochemical nitrogen fixation under ambient conditions, J. Mater. Chem. A **10**, 13527 (2022).

[33] J. Wang, B. Chen, and B. Xing, Wrinkles and folds of activated graphene nanosheets as fast and efficient adsorptive sites for hydrophobic organic contaminants, Environ. Sci. Technol. **50**, 3798 (2016).

[34] M. Sahoo and S. Ramaprabhu, Effect of wrinkles on electrochemical performance of multiwalled carbon nanotubes as anode material for Li ion battery, Electrochim. Acta **186**, 142 (2015).